Simulating Realistic Synthetic Longitudinal Brain MRIs with known Volume Changes

Bishesh Khanal, Nicholas Ayache, Xavier Pennec

Simulating Realistic Synthetic Longitudinal Brain MRIs with known Volume Changes

Bishesh Khanal[1,*], Nicholas Ayache[1,*], Xavier Pennec[1,*]

Abstract

This paper presents a simulator tool that can simulate large databases of visually realistic longitudinal MRIs with known volume changes. The simulator is based on a previously proposed biophysical model of brain deformation due to atrophy in AD. In this work, we propose a novel way of reproducing realistic intensity variation in longitudinal brain MRIs, which is inspired by an approach used for the generation of synthetic cardiac sequence images. This approach combines a deformation field obtained from the biophysical model with a deformation field obtained by a non-rigid registration of two images. The combined deformation field is then used to simulate a new image with specified atrophy from the first image, but with the intensity characteristics of the second image. This allows to generate the realistic variations present in real longitudinal time-series of images, such as the independence of noise between two acquisitions and the potential presence of variable acquisition artifacts. Various options available in the simulator software are briefly explained in this paper. In addition, the software is released as an open-source repository. The availability of the software allows researchers to produce tailored databases of images with ground truth volume changes; we believe this will help developing more robust brain morphometry tools. Additionally, we believe that the scientific community can also use the software to further experiment with the proposed model, and add more complex models of brain deformation and atrophy generation.

Keywords:. Neurodegeneration, biophysical modelling, biomechanical simulation, simulated database, synthetic images, synthetic longitudinal MRIs

1. Introduction

Structural Magnetic Resonance Imaging (MRI) has been widely used for in-vivo observation of morphological changes over time in human brain. Atrophy or tissue volume loss measure from structural MRI is an established biomarker for neurodegeneration (Frisoni et al., 2010). There is a large number of brain morphometry algorithms developed in the

*Corresponding author
Email address: bishesh.khanal@inria.fr (Bishesh Khanal)
[1]INRIA Sophia Antipolis Méditerranée, Asclepios Research Project

literature which estimate global or local atrophy from structural MRIs (Wright et al., 1995; Freeborough and Fox, 1997; Ashburner and Friston, 2000; Smith et al., 2002; Hua et al., 2008). Volume/atrophy measurements obtained from such algorithms have been used to test various clinical hypotheses about neurodegenerative diseases (Wright et al., 1995; Sepulcre et al., 2006; Koch et al., 2016). Similarly, comparison of different neurodegenerative diseases have also been performed based on these measurements (Rosen et al., 2002; Whitwell and Jack Jr, 2005). Since atrophy estimation is an inverse problem, the estimation algorithms require a model with certain parameters. The results obtained from such algorithms depend on model assumptions and the parameters used. Often, these assumptions are implicit and cannot be directly linked to the biophysical process of neurodegeneration. For instance, tensor based morphometry (TBM) encodes local volume changes by computing Jacobian determinants of the deformation field obtained from non-linear registration of longitudinal MRIs (Ashburner and Ridgway, 2015). Such methods contain model biases because TBM results depend on the choices of regularization used during the registration of images (Ashburner, 2013). Estimating and correcting the bias present in such morphometry tools is important, especially for clinical applications.

In addition to tracking volumetric changes in specific brain structures, longitudinal imaging data can also be used to study the temporal inter-relationship of atrophy in different structures. For instance, Carmichael et al. (2013) studied the groupings of 34 cortical regions and hippocampi from the per-individual rates of atrophy estimates in these regions. In Fonteijn et al. (2012), authors defined AD progression as a series of discrete events. Along with other clinical events, the timings of atrophy in various brain structures were included in a set of discrete events. Without any prior to their ordering, the model finds the most probable order for these events from the data itself. They used Bayesian statistical algorithms for fitting the event-based disease progression model. The objective of these studies were to understand how different regions of brain evolve during the neurodegeneration.

In this context of increasing use of the atrophy measurements from longitudinal MRIs in testing or discovering clinically relevant hypotheses, it is important to study the bias and variability of the atrophy estimation algorithms. The actual volume changes in real longitudinal MRIs are not known. Thus, the evaluation and validation of atrophy estimation algorithms require generating images with known volume changes, called ground truth images.

A number of atrophy simulators have been proposed in the literature to produce ground truth MRIs (Smith et al., 2003; Camara et al., 2006; Karaçali and Davatzikos, 2006; Pieperhoff et al., 2008; Sharma et al., 2010; Khanal et al., 2016a). These simulators use a model that attempts to produce a deformation field with the specified volume changes in the input brain MRI. To produce realistic scenarios of noise and acquisition artifacts, some of these simulators also use a model to produce noise and artifacts in the simulated image.

Such simulators have been used for the validation of registration or segmentation based atrophy estimation algorithms (Camara et al., 2008; Pieperhoff et al., 2008; Sharma et al., 2010), to estimate the bias in such algorithms, and also to estimate uncertainty in the measured atrophy (Sharma et al., 2013). These studies have estimated the bias by simulating simple atrophy patterns in a small number of brain regions, or uniform diffused global

atrophies. However, real case scenarios could have a much more complex atrophy distribution occurring in many brain structures at the same time.

Noise and imaging artifacts have an important impact on the results obtained from atrophy estimation algorithms (Pieperhoff et al., 2008; Camara et al., 2008; Sharma et al., 2010). Thus, proper evaluation of atrophy estimation algorithms by using simulated ground truth images requires simulation of realistic variation in noise and intensity too. All the previous atrophy simulators have warped the input baseline image with the deformation field obtained from a model of brain deformation. Then, extra noise and artifacts are added on this warped image by using another artificial model. The intensity noise in structural MRIs has been shown to be governed by a Rician distribution where the noise is Gaussian in k-space (Gudbjartsson and Patz, 1995). Thus the Rician noise can be added in the simulated images as follows:

- Use two independent random variables following zero-mean Gaussian distribution to compute the real and imaginary parts of a complex number at each voxel.
- Add the magnitude of this complex number to the intensity of the simulated MRI at each voxel.

For example, Sled et al. (1998) used this approach to add noise in simulated MRIs that were used for the validation of intensity bias correction scheme they presented. Using the same approach, Camara et al. (2008) added noise to the simulated ground truth images with atrophy. In addition to the Rician noise described above, other noise and artifacts have also been shown to affect the measurements of atrophy estimation algorithms (Sharma et al., 2010; Pieperhoff et al., 2008):

- Bias field inhomogeneity arising due to poor radio frequency (RF) coil uniformity.
- Geometrical distortions that are present due to the errors in gradient field strength and non-linearity of gradient fields in the MR scanner (Langlois et al., 1999).
- Interpolation of intensities during various pre-processing steps of TBM based analysis framework (e.g., resampling of the images into a common template space).

Many other acquisition artifacts may not be simulated because we do not have faithful models. In this work, we develop a new framework to simulate longitudinal images with specified volume changes, and also the realistic intensity variations including the noise and acquisition artifacts. In the framework, we use our biophysical model of brain deformation (Khanal et al., 2016a) to obtain a dense deformation field with specified volume changes. To obtain the realistic intensity variations, we use an approach introduced by Prakosa et al. (2013) where the authors simulate visually realistic time series of cardiac images. Intensity variation in the simulated images of a patient is obtained by resampling the intensities from real images of the same patient taken at different times. Figure 1 shows a diagram of this framework. To implement this framework, we have developed an open-source atrophy simulator software called `Simul@trophy`[2].

[2]Available at `https://team.inria.fr/asclepios/software/` under acceptance.

Section 2 explains all the blocks of the framework shown in Figure 1. Starting from a small set of real scans, we show how longitudinal images with different atrophy patterns and realistic intensity variations can be simulated. Section 3 shows some simulation results using `Simul@trophy`, and also illustrates some potential applications of the simulator. In Section 4, we present some example simulations to illustrate some of the important points to consider when using `Simul@trophy` for different applications, such as evaluation of atrophy estimation algorithms, validation of data-driven disease progression models, training of brain morphometry algorithms based on machine learning etc.

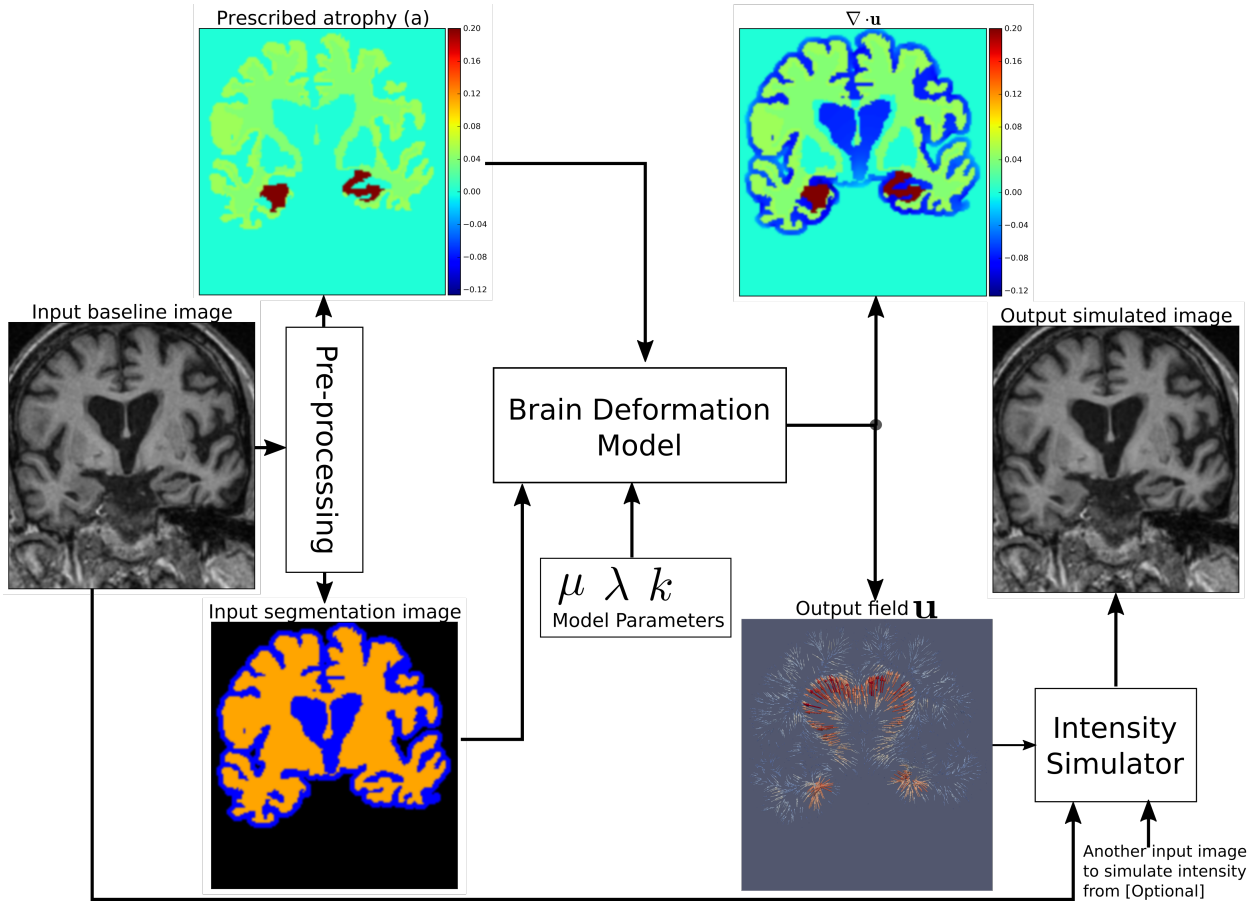

Figure 1: Pipeline to simulate synthetic images using `Simul@trophy`. Starting from a real baseline image of a subject, synthetic images with known volume changes can be generated. These synthetic images can follow intensity characteristics of either the input baseline or other images of the same subject. Pre-processing is required to generate an atrophy map and a segmentation image, which are fed as inputs to the brain deformation model. For a given set of parameters, the model computes a velocity field whose divergence is equal to the prescribed atrophy map at each voxel of the regions selected by using the segmentation image. Intensity simulator uses the output field to produce synthetic image whose intensity is resampled either from the input real baseline or from any other image as desired.

2. Simulating Realistic Longitudinal Images with Atrophy/Growth

We use the biophysical model presented in Khanal et al. (2014, 2016a) to generate dense deformation field with specified complex patterns of volume changes. This deformation field is then used to generate realistic synthetic longitudinal images with intensity variation, noise and artifacts, just like in real longitudinal images. The major components of the simulation framework, as seen in Figure 1, are: i) Pre-processing ii) Brain deformation model iii) Realistic intensity simulator.

2.1. Pre-processing to generate a segmentation image and atrophy maps

A pre-processing step takes a real scan of a patient as an input baseline image, and generates the required inputs of the brain deformation model: a segmentation image and a specified atrophy map.

2.1.1. Segmentation Image

There are three labels in the segmentation image used by `Simul@trophy` (Figure 1):

- `Label0`: regions where no deformation should be prescribed,
- `Label1`: regions where certain volume changes are prescribed (the values of volume changes are provided with an input atrophy map),
- `Label2`: regions where the deformation model is allowed to adapt volume changes as required to compensate for the total volume change prescribed in regions with `Label1`.

Pre-processing usually starts with a brain extraction that excludes the skull and outside regions (also called skull stripping). Skull stripping is followed by a segmentation such that each voxel of the input image could be assigned to one of the three labels. For example, a typical pre-processing step that includes a segmentation of brain parenchyma and CSF would produce a segmentation image with the following labels:

- `Label0`: Skull and outside regions of the input image
- `Label1`: Gray and white matter regions
- `Label2`: CSF regions

2.1.2. Atrophy map

An atrophy map is a scalar image with desired values of volume changes in `Label1` regions of the segmentation image, and zeros in all the other regions. It is defined at each voxel as follows:

$$a = \frac{V_0 - V_1}{V_0},$$

where V_0 and V_1 are the volumes of the material lying in a voxel at time t_0 and t_1 respectively. Thus, regions with volume loss have positive values of a while the regions with volume expansion have negative values of a. An example atrophy map is shown in Figure 1.

In this work, we illustrate example simulations where two kinds of pre-processing steps were used to generate the atrophy maps:

Segmentation based atrophy map

The user can set uniform values of atrophy in regions of interests (ROIs) of the brain. In this case, one must first perform a segmentation of all ROIs in which a non-zero value of atrophy is desired. Then, it is straightforward to create a scalar image having intensity values taken from a table, which contains the labels of ROIs and the corresponding desired atrophy values.

Registration based atrophy map

The results of longitudinal non-rigid registration can be used to estimate local volume changes, for instance by computing Jacobian determinants of the displacement fields or by computing the divergence of the stationary velocity fields obtained from the registration. These local volume changes obtained from the registration based methods are usually smoothly varying in space and can be used to prescribe either:

- smoothly varying atrophy maps,
- or atrophy maps uniform in ROIs obtained by averaging, in each ROIs, the atrophy obtained above.

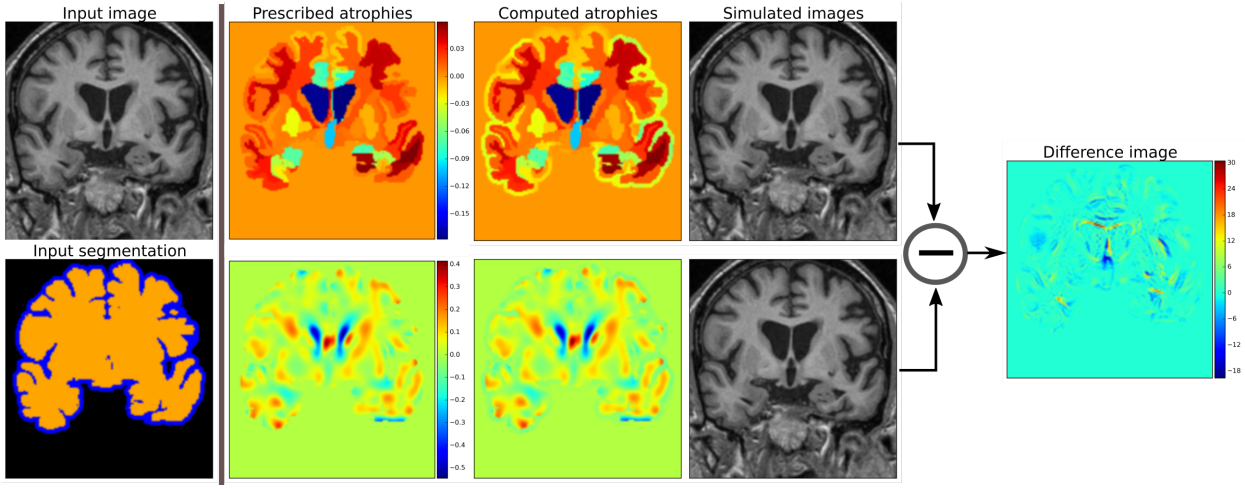

Figure 2: Examples of two different kinds of atrophy maps. The first row prescribes atrophy map that is uniform in different regions of the brain, while the second row prescribes smoothly varying atrophy. Both of these atrophy maps have same average values in each ROIs. The example also shows that we can prescribe volume changes in ventricles, if desired, by adapting the input segmentation map accordingly. The simulated images, as shown, are different although they have same mean regional atrophy values.

Figure 2 shows two such atrophy maps with very different patterns, but having the same average regional volume changes.

2.2. A biophysical model of brain deformation with prescribed volume changes

`Simul@trophy` uses the biomechanics based model of brain deformation detailed in Khanal et al. (2016a). The model abstracts the phenomenon that evolves during several

months or years in the brain at a macroscopic scale. It is based on the assumption that atrophy creates an internal stress which results in the deformation minimizing a strain energy. In other words, the brain parenchyma deforms with the prescribed atrophy by minimizing the strain energy. By taking a sufficiently small time step Δt, this deformation could be reasonably modeled as being linear elastic. For example, for a 2% global atrophy rate per year, we have $\Delta t = 1\,year$, and the actual atrophy after one year is $a = 0.02$.

For a given segmentation image, the model yields a deformation field with the prescribed atrophy at each voxel of `Label2` regions (e.g. brain parenchyma). `Label1` regions (e.g. the CSF) will correspondingly adapt its volume to globally compensate for the prescribed volume changes in the `Label2` regions. For a single time-step, the displacement field $\mathbf{u}$ is obtained by solving the system of Eqs 1, where Dirichlet boundary conditions of zero deformation are prescribed in `Label0` regions.

$$\left.\begin{array}{l}\text{Regions with: } \texttt{Label0}\\ \mathbf{u} = 0\\ \text{Dirichlet boundary conditions}\end{array}\right\} \quad \left.\begin{array}{l}\texttt{Label1}\\ \mu\Delta\mathbf{u} - \nabla p = 0\\ \nabla\cdot\mathbf{u} + kp = 0\end{array}\right\} \quad \left.\begin{array}{l}\texttt{Label2}\\ \mu\Delta\mathbf{u} - \nabla p = (\mu+\lambda)\nabla a\\ \nabla\cdot\mathbf{u} \quad\quad = -a\end{array}\right\} \tag{1}$$

The system of Eqs. 1 shows that the incompressibility constraint is relaxed in `Label1` regions, while it is strictly satisfied in `Label2` regions. The impact of the choice of different values for the model parameters μ, λ and k are detailed in Khanal et al. (2016a). For the same prescribed volume changes, we can obtain different deformation fields by varying these model parameters. In this work, we focus on generating ground truth images with known volume changes and not necessarily generating the exact evolution of the AD patients. Hence, we set the model parameters as follows unless specified otherwise: $\mu = 1$ kPa, $\lambda = 0$ kPa, $k = 1$ kPa^{-1}.

Once the field $\mathbf{u}$ with the prescribed volume changes is obtained from the model as described above by using an input baseline image I_b, we can simulate a synthetic follow-up image I_s as follows:

- Let $\mathbf{y} = \Phi_{\text{sim}}(\mathbf{x}) = \mathbf{u} + \mathbf{x}$ describe a mapping of a point $\mathbf{x}$ in physical space to another point $\mathbf{y}$ by applying the transformation corresponding to the dense deformation field Φ_{sim}, or the displacement field $\mathbf{u}$.
- Let $\Phi_{\text{sim}} \star I_b$ describe an action of the diffeomorphism Φ_{sim} on the image I_b. Thus, the new synthetic image I_s, obtained by warping I_b with the deformation field Φ_{sim} is given by:
$$I_s = \Phi_{\text{sim}} \star I_b = I_b \circ \Phi_{\text{sim}}^{-1}.$$

Figure 2 shows two simulated images from the same input baseline image but with two different atrophy patterns.

2.3. Adding realistic intensity variation to synthetic longitudinal MRIs

In realistic scenarios, longitudinal MRIs are taken at multiple scan sessions often with slightly different acquisition parameters or even with different scanners. For generating more

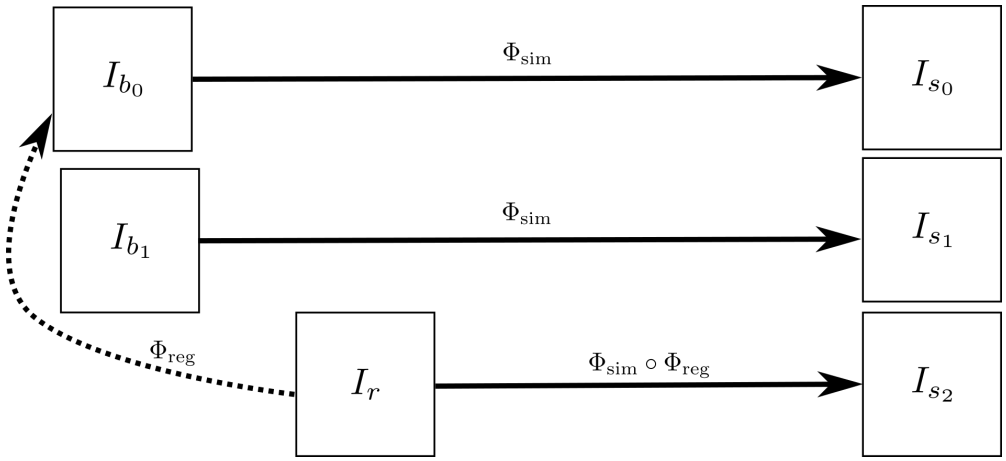

Figure 3: I_{b_0} and I_{b_1} are the repeat scans of a subject taken within a short period of time during which there is no morphological changes in the brain of the subject. I_r is taken at a later time when the brain could have undergone some morphological changes. The deformation field Φ_{reg} is obtained by registering I_r to I_{b_0}, while Φ_{sim} is obtained from the brain deformation model using I_{b_0} as the input image. The three simulated images I_{s_0}, I_{s_1} and I_{s_1} are all same time-point images but have different intensities that come from I_{b_0}, I_{b_1} and I_r respectively.

realistic synthetic longitudinal MRIs, variations in intensity and noise present in real longitudinal MRIs must also be simulated. If multiple repeat scans of a subject are available, we can use them to simulate such variations in synthetic longitudinal sequences. Assuming that all the available scans of the subject are already aligned using affine registration, this section explains the proposed method of adding realistic variations in the intensity characteristics.

Starting from an input baseline image I_{b_0} of a subject, the previous sections explained how we can obtain a deformation field Φ_{sim} from the brain deformation model, and use it to simulate a follow-up image

$$I_{s_0} = \Phi_{\text{sim}} \star I_{b_0}.$$

I_{s_0} has the same intensity characteristics as I_{b_0}, and the intensity noise in I_{s_0} is strongly correlated to the noise present in I_{b_0}.

If I_{b_1} is another scan of the same subject taken on the same day, we can obtain a new simulated image by resampling the intensity from I_{b_1}, but still using the same Φ_{sim}:

$$I_{s_1} = \Phi_{\text{sim}} \star I_{b_1}$$

The realistic variation of intensity and artifacts present between the two real scans I_{b_0} and I_{b_1} are now also present between the real baseline image I_{b_0} and the simulated follow-up image I_{s_1}.

The above approach assumes that the brain has not gone any morphological changes between the scan sessions of the two real images. If the scan time-points of the two images are too far apart to have this assumption valid, we can no longer directly apply Φ_{sim} to the second image. Let I_r be another real scan of the patient taken at a time later than that of the baseline image I_{b_0}. There might be some morphological changes (e.g. atrophy) in I_r compared to I_{b_0}.

To simulate a new synthetic image with the same atrophy as that of I_{s_0} but with the intensity resampled from I_r, we must first perform a non-rigid registration between I_r and I_{b_0}. If Φ_{reg} is the deformation field obtained from the non-rigid registration between I_r and I_{b_0}, it can be used to get an image $\Phi_{\text{reg}} \star I_r$ which is aligned to I_{b_0}. In the ideal case, $\Phi_{\text{reg}} \star I_r$ and I_{b_0} are perfectly aligned with the only differences lying in the intensity characteristics and the noise.

We can now compose the deformation fields Φ_{sim} and Φ_{reg} to generate a new synthetic image as follows:

$$I_{s_2} = (\Phi_{\text{sim}} \circ \Phi_{\text{reg}}) \star I_r.$$

I_{s_2} has the same atrophy as that of I_{s_0} but with the intensity characteristics of I_r. Figure 3 illustrates how we obtain I_{s_0}, I_{s_1} and I_{s_2}. These three simulated images have the volume changes as encoded by Φ_{sim}, but have intensity characteristics coming from three different real images of the same patient.

Figure 4 illustrates how the approach described in this section can be used to generate multiple sets of longitudinal simulated sequences having identical morphological evolution but different variations of intensities. The three shaded regions in Figure 4 are the sets of longitudinal sequences with identical volume changes but with different variations of intensities.

3. Simulation Examples with `Simul@trophy`

This section presents simulation examples of synthetic longitudinal MRIs with prescribed atrophy patterns and realistic intensity variations [3]. The real input MRIs used for the simulations presented in this section were obtained from the publicly available OASIS dataset (Marcus et al., 2010). All these real MRIs had undergone intensity inhomogeneity correction using `ANTs - N4BiasFieldCorrection` (Avants et al., 2011), and had been transported to a common space using affine registration with `FSL - FLIRT` (Jenkinson and Smith, 2001). More precisely, these images had undergone the `Pre-Processing` and `Position Correction` steps of the Longitudinal Log-Demons Framework (LLDF) detailed in Hadj-Hamou et al. (2016).

Figure 5 shows a simulation example where uniform atrophy patterns are prescribed in the hippocampi, the gray matter (GM), and the white matter (WM) regions. The ventricles and sulcal CSF regions are allowed to expand as required to compensate for the volume loss in the brain parenchyma. The figure shows two simulated images whose intensities are resampled from two different images: i) the input baseline image I_b ii) another follow-up image of the same subject, I_r. The figure also shows intensity histograms of these two simulated images for a selected ROI. The selected ROI is a 2D WM region where the simulated images do not have a distinct morphological changes from I_b. Thus, the differences in the intensity histograms of I_b and the simulated images for this ROI is mostly due to the

[3] The simulation results are made available at `http://neurovault.org/collections/AUKWWYBC/` (Gorgolewski et al., 2015).

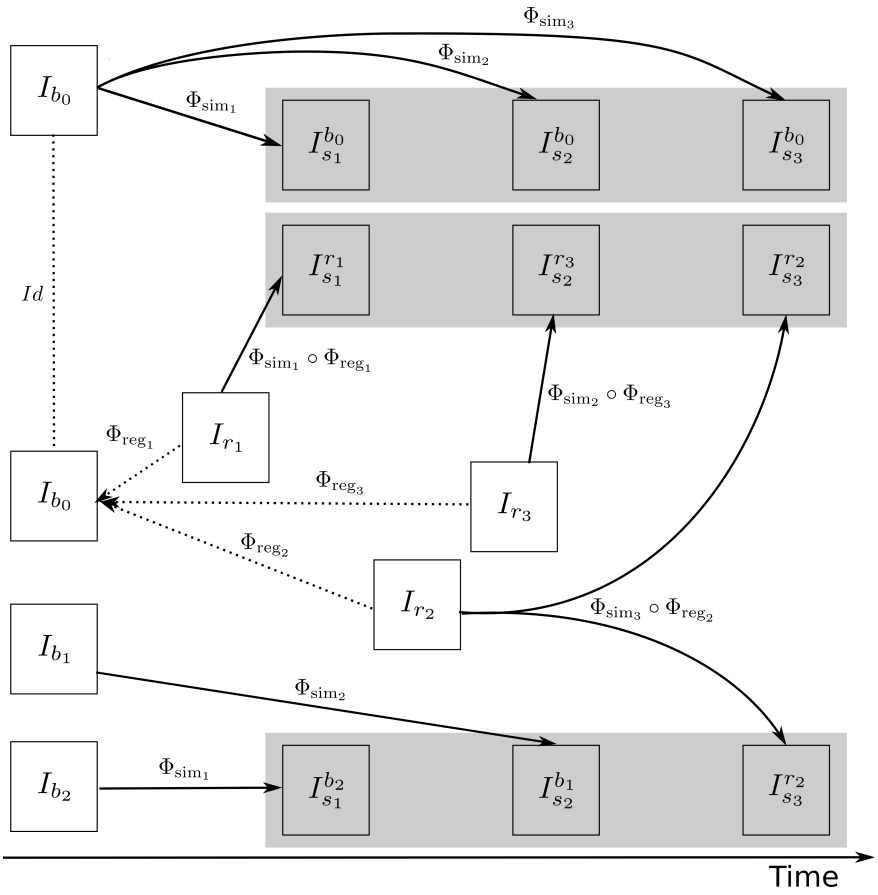

Figure 4: A general approach to simulate ground truth synthetic longitudinal images with realistic intensity variations; simulated images are shown within the shaded regions. The deformation fields with a prescribed atrophy for three time-points (Φ_{sim_1}, Φ_{sim_2}, and Φ_{sim_3}) are obtained from the biophysical model using I_{b_0} as the input baseline image. Several different sets of longitudinal images can then be simulated by resampling intensities from different combinations of available real images. The topmost shaded region shows a longitudinal sequence with no realistic intensity variations where the synthetic images are all resampled from I_{b_0}. The remaining two shaded regions have longitudinal sequences with realistic intensity variations where the simulated images are resampled from other available images of the same subject. In the ideal case, the three sets of longitudinal sequences have exactly the same morphological changes but with different variations in intensity characteristics.

variation in intensity characteristics of the different images. We can see from the figure that the intensity characteristics of the simulated image resampled from I_b closely matches the intensity characteristics of I_b. And resampling the intensity from a different image I_r of the same subject allows simulating realistic variation of intensities.

To simulate multiple time-point images, the following approach can be used:

- Get $\mathbf{u}_0$ by solving the system of Eqs. (1) using the initial atrophy map a_0 and the initial segmentation image L_0 as input.
- For each time step $t = 1$ to n:

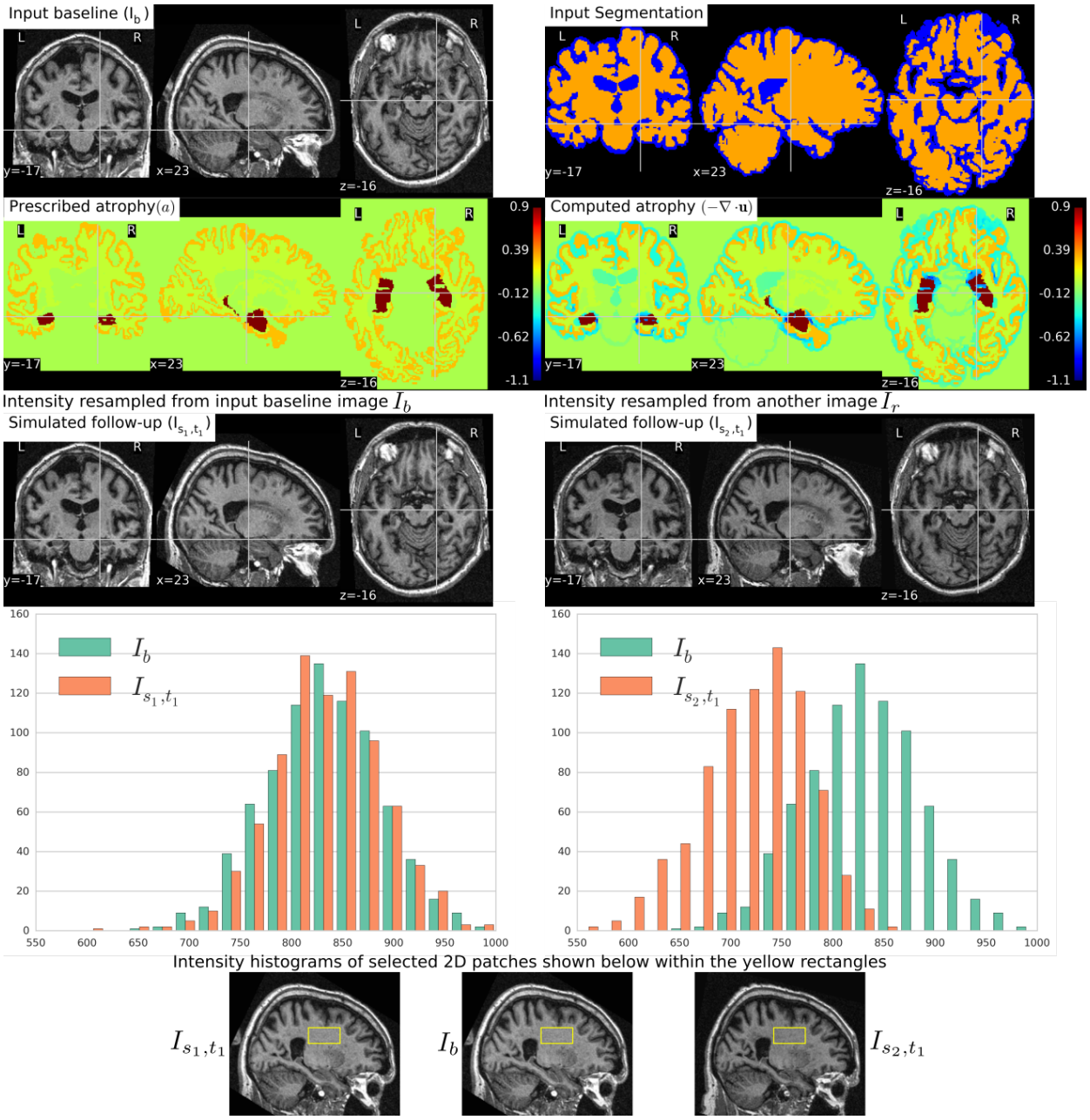

Figure 5: Two simulated images are shown on the third row where the image on the left is resampled from the input baseline image I_b, and the image on the right is resampled from another image I_r of the same subject. Both I_b and I_r had already been corrected for the bias field intensity inhomogeneity. The intensity histograms shown are of a selected ROI (shown on the last row) where there is no significant morphological changes between the images. From the histograms we can see that the simulated image I_{s_2,t_1} has a different intensity characteristics than I_b, while the simulated image I_{s_1,t_1} has intensity characteristics that closely matches to that of I_b.

– Warp a_{t-1} and L_0 using $\mathbf{u}_{t-1} \circ \mathbf{u}_{t-2} ... \circ \mathbf{u}_0$ to get a_t and L_t respectively.

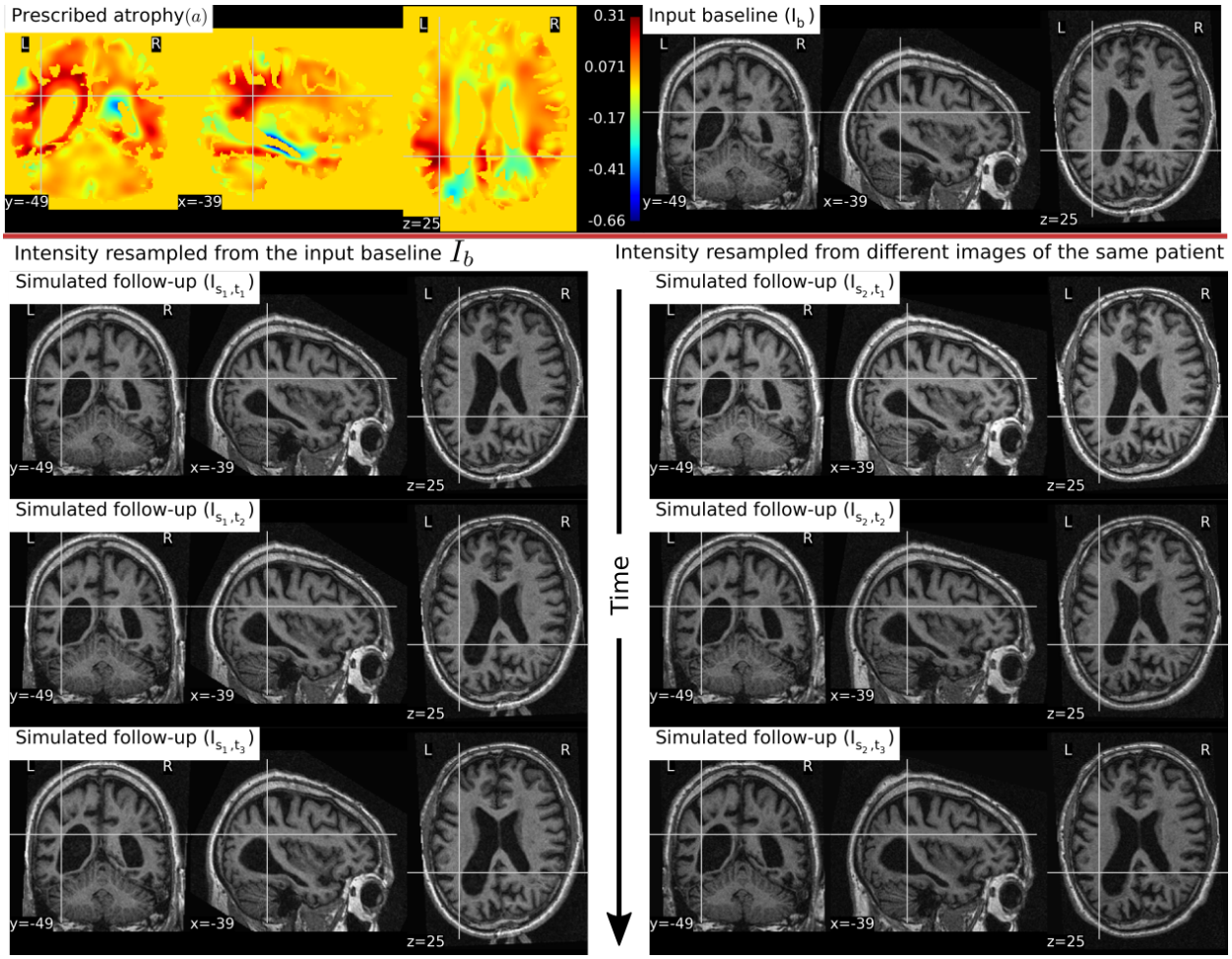

Figure 6: Two sets of synthetic longitudinal images are shown which are simulated by prescribing a smoothly varying atrophy pattern. The first row shows the input prescribed atrophy and the input baseline image I_b of a subject, while the remaining rows show the two sequences. The sequence shown on the left have simulated images that are all resampled from I_b. On the right, each simulated image is resampled from real MRIs of the same subject but taken at different times. As shown by the intensity histograms of Figure 7, the longitudinal synthetic images on the right have more realistic intensity variations than the one left.

– Solve for $\mathbf{u}_t$ using a_t and L_t as input.

Once all the deformation fields Φ_{s_i} corresponding to $\mathbf{u}_i$ for $i = 0, 1, ..., n$ are obtained, these deformation fields can be used as shown in Figure 4 to simulate different sequences of longitudinal images.

In Figure 6, a simulation example of two longitudinal sequences each having three new time-point images is shown. Both sequences were simulated by prescribing a smoothly varying atrophy pattern. The smoothly varying atrophy pattern prescribed in this example is more complex than the simple pattern used in the previous example. It is adapted from the divergence of a stationary velocity field obtained by performing LCC log-Demons registration (Lorenzi et al., 2013) of the input baseline image with a follow-up image of the same subject.

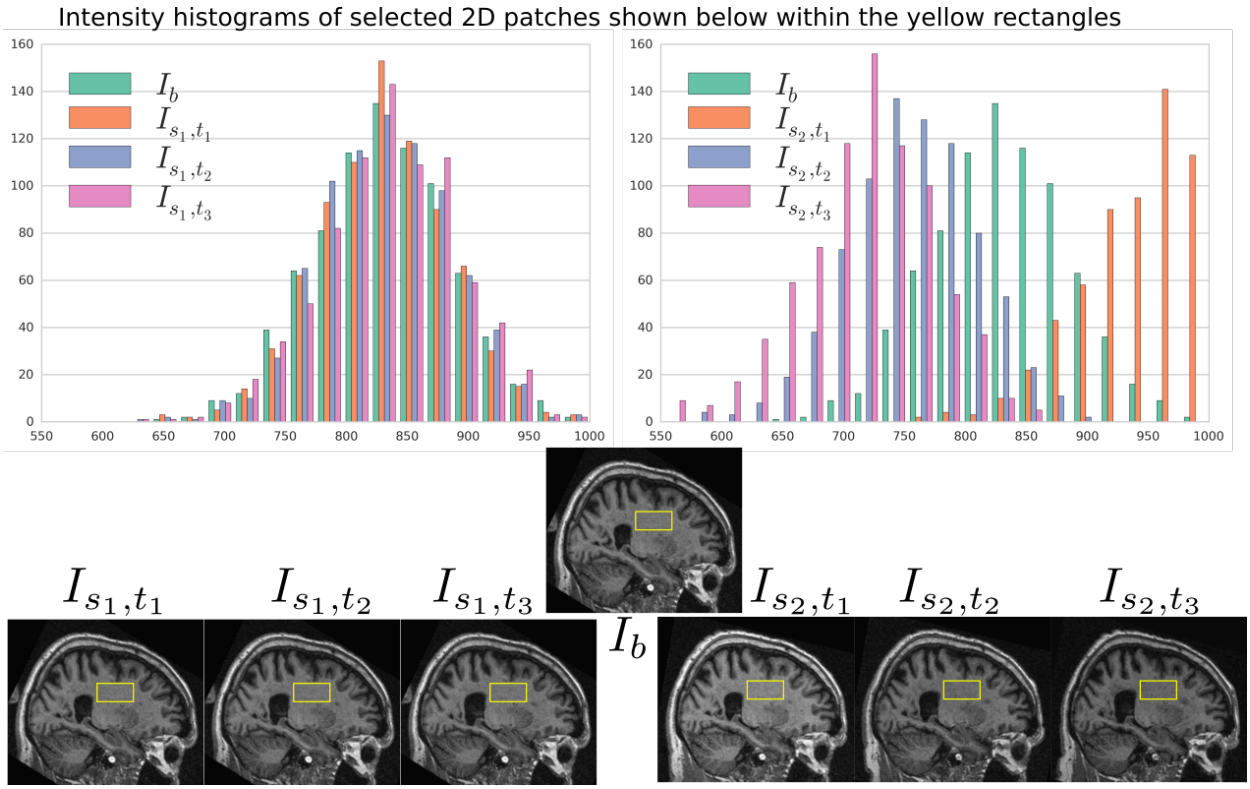

Figure 7: Intensity histograms of selected patches of the images simulated in Figure 6. When the simulated images are resampled from the same input baseline image I_b, as expected, the histograms of the simulated images closely match with each other. However, when simulated images are resampled from other different images of the same patients, the histograms of these simulated images do not match closely. The longitudinal sequence of simulated images I_{s_2,t_1}, I_{s_2,t_2} and I_{s_2,t_3} has realistic variation in intensities as observed in the real sequences.

The first sequence consists of all the images whose intensities are resampled from the same input baseline image I_b, while the second sequence consists of the images whose intensities are resampled from different real MRIs of the same subject. Thus, as shown in Figure 7, the first sequence does not have the realistic variation of intensities while the second sequence has the realistic variation of intensities. With this example, we also illustrated that we can generate multiple sequences of longitudinal images with same atrophy patterns but different variations of intensities.

Figure 8 shows a simulation example where we prescribe growth instead of atrophy in the brain tissue. The prescribed atrophy in this case is the negative of the atrophy map prescribed in Figure 6. From the segmentation image shown in Figure 8, we can see that the ventricles were allowed to adapt the volume changes as required to compensate for the volume changes in the brain parenchyma. From the three simulated time-points, we can see that these ventricles are shrinking and the brain parenchyma regions are expanding. The example shows that `Simul@trophy` can be used to simulate images of not only future time-points, but also the past time-point images.

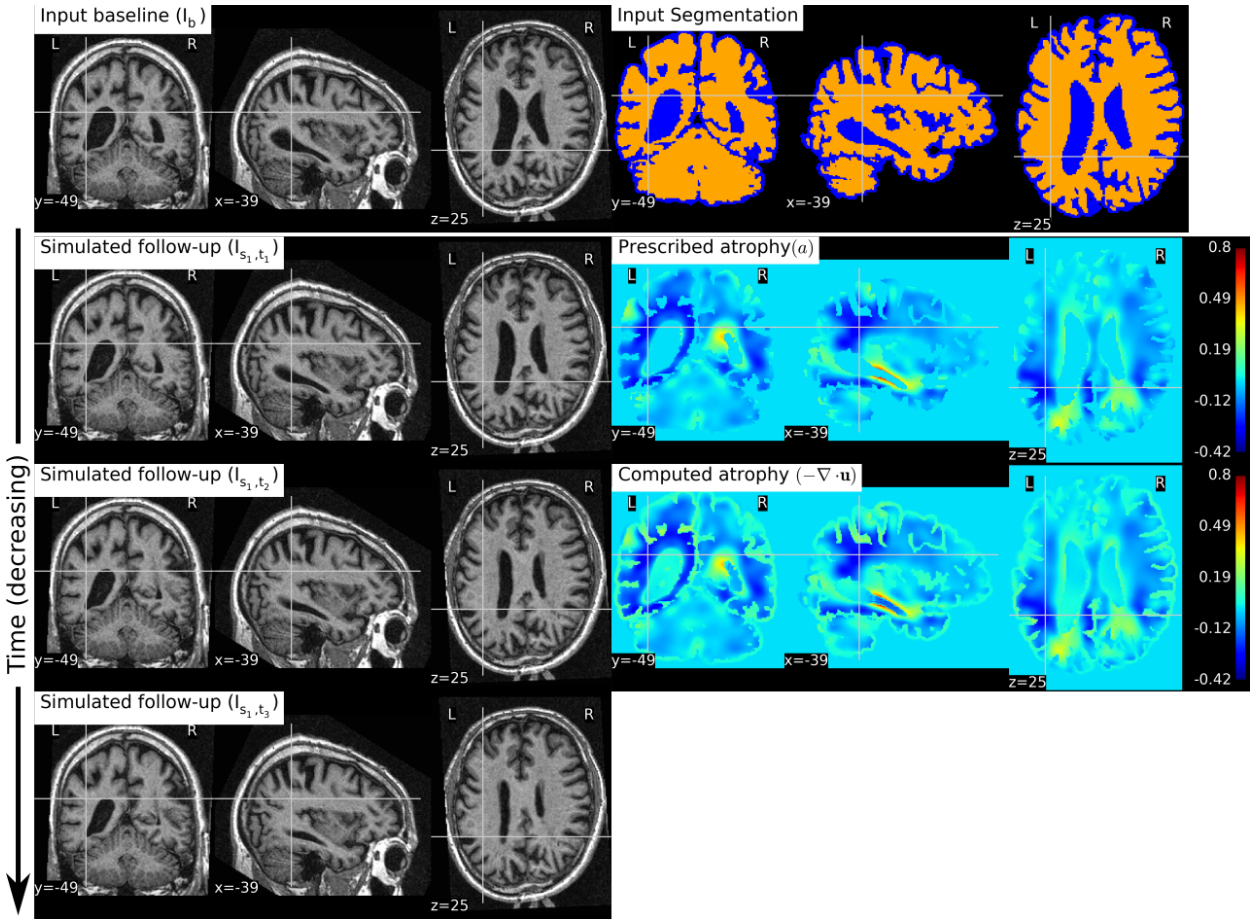

Figure 8: The figure shows an example of simulating a longitudinal sequence with backward time-points. The input baseline image I_b is the same one as used in Figure 6, and the prescribed atrophy map is the negative of the map used in Figure 6. In the figure, we can see the shrinkage of the ventricles and the growth of the brain parenchyma.

In Figure 9, we show an example where synthetic sequence of images is simulated by starting from a baseline image of a healthy subject. However, the prescribed atrophy is derived from an atrophy estimated from the AD patient used in Figure 6. The input baseline images of both the AD patient and the healthy subject were segmented using FreeSurfer (Fischl et al., 2002). In all the segmented regions including the white matter parcellations of the AD patient, the average values of the smoothly varying atrophy map were computed. These regional average values of the atrophy computed from the AD patient were then transported to the corresponding regions of the healthy subject. Thus, in Figure 9, we can see that the prescribed atrophy is region-wise uniform instead of smoothly varying. For comparison, the figure also shows three real time-point images of the healthy subject along with the three simulated time-point images with atrophy derived from the AD patient.

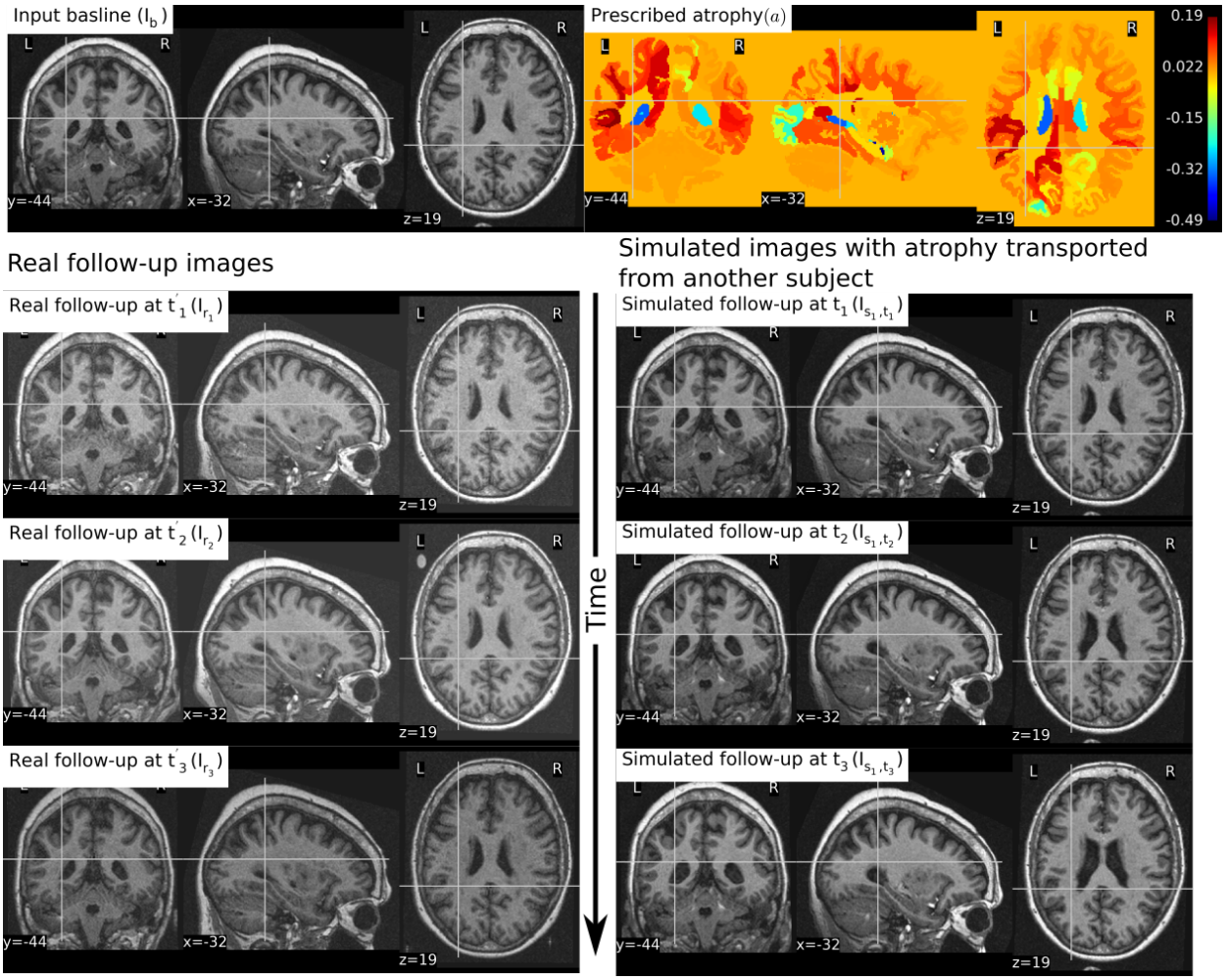

Figure 9: The figure shows an example of simulating follow-up images of a normal subject with baseline image I_b, where the prescribed atrophy pattern is adapted from an AD patient. The prescribed atrophy is adapted from the atrophy estimated for the AD patient shown in Figure 6. Average values of the smoothly varying prescribed atrophy shown in Figure 6 is computed in all the ROIs. The ROIs are obtained from the FreeSurfer segmentation including all the white matter parcellations (Fischl et al., 2002). The simulated images on the right have bigger shrinkage of the brain parenchyma and bigger expansion of the ventricles than the real images on the left.

4. `Simul@trophy`: choices available and practical considerations

`Simul@trophy` is available as an open-source repository under git version control. Researchers can use it according to their needs, improve the presented model, and/or add new models of brain atrophy. It is based on two core components: i) The Insight ToolKit (ITK) and ii) PETSc Balay et al. (2013). All the input and output images of the brain deformation model shown in Figure 1 can be in any format that ITK supports. ITK has strongly promoted reproducible science in the medical imaging domain, and has been widely used in computational science applied to medical imaging (McCormick et al., 2014; Avants

et al., 2015). Similarly, implementation of the model solver is based on open-source PETSc, a library based on C programming language. It has also been very widely used in a very diverse set of applications that also include the medical field. It is a very powerful library that supports wide range of iterative solvers and preconditioners for large systems of equations. The solvers implemented in PETSc can scale very well to large distributive computer systems.

`Simul@trophy` runs from command lines where the required inputs and optional choices are provided via command line arguments. The available command lines are detailed in Appendix 7. In this section, we illustrate some examples of how certain choices made during the simulation affect output results.

4.1. Impact of registration on simulated images

In Section 2.3, we explained that starting from an input baseline image of a subject, I_b, we can generate two synthetic images:

$$I_{s_1} = \Phi_{\text{sim}} \star I_f \qquad \text{and} \qquad I_{s_2} = (\Phi_{\text{sim}} \circ \Phi_{\text{reg}}) \star I_f$$

where Φ_{sim} is the deformation field obtained from the brain deformation model using I_b as the input baseline image, and Φ_{reg} is the deformation field obtained from the non-rigid registration between I_b and a real follow-up image I_f. Perfect alignment of the two images with a non-rigid registration is possible only in the ideal case scenario. In such an ideal case, the simulated images I_{s_1} and I_{s_2} have identical shapes of the brain structures with the only differences lying in the intensity characteristics. In practice, this is almost never the case, and we present below an example of the impact of registration result on the simulated images.

Let us use the following short notations for various images described in this section.

- `RB`: Real baseline image: I_b
- `RF`: Real follow-up image: I_f
- `RB_to_RF`: Real baseline aligned to real follow-up: $\Phi_{\text{reg}}^{-1} \star I_b$
- `SF_in_RB`: Simulated follow-up image with intensity resampled from I_b: $\Phi_{\text{reg}}^{-1} \star I_b$
- `SF_in_RF`: Simulated follow-up image with intensity resampled from I_f: $(\Phi_s \circ \Phi_{\text{reg}}) \star I_f$

Figure 10 illustrates the impact of registration result Φ_{reg} on the simulation results. The figure shows both the registration and simulation results along with zoomed patches of `RB`, `RB_to_RF`, `SF_in_RB` and `SF_in_RF`. As expected, `SF_in_RB` and `SF_in_RF` have different intensity characteristics coming from `RB` and `RF` respectively. In the regions where registration is accurate, the two simulated images look almost identical except for the differences in the intensity characteristics. However, in the regions where registration is not accurate enough, `SF_in_RB` and `SF_in_RF` do not have identical shapes as expected. Thus, for the proposed method of using deformations obtained by registration for simulation, it might be preferable to use aggressive non-linear registrations with a much bigger weight given to similarity terms than the regularization terms.

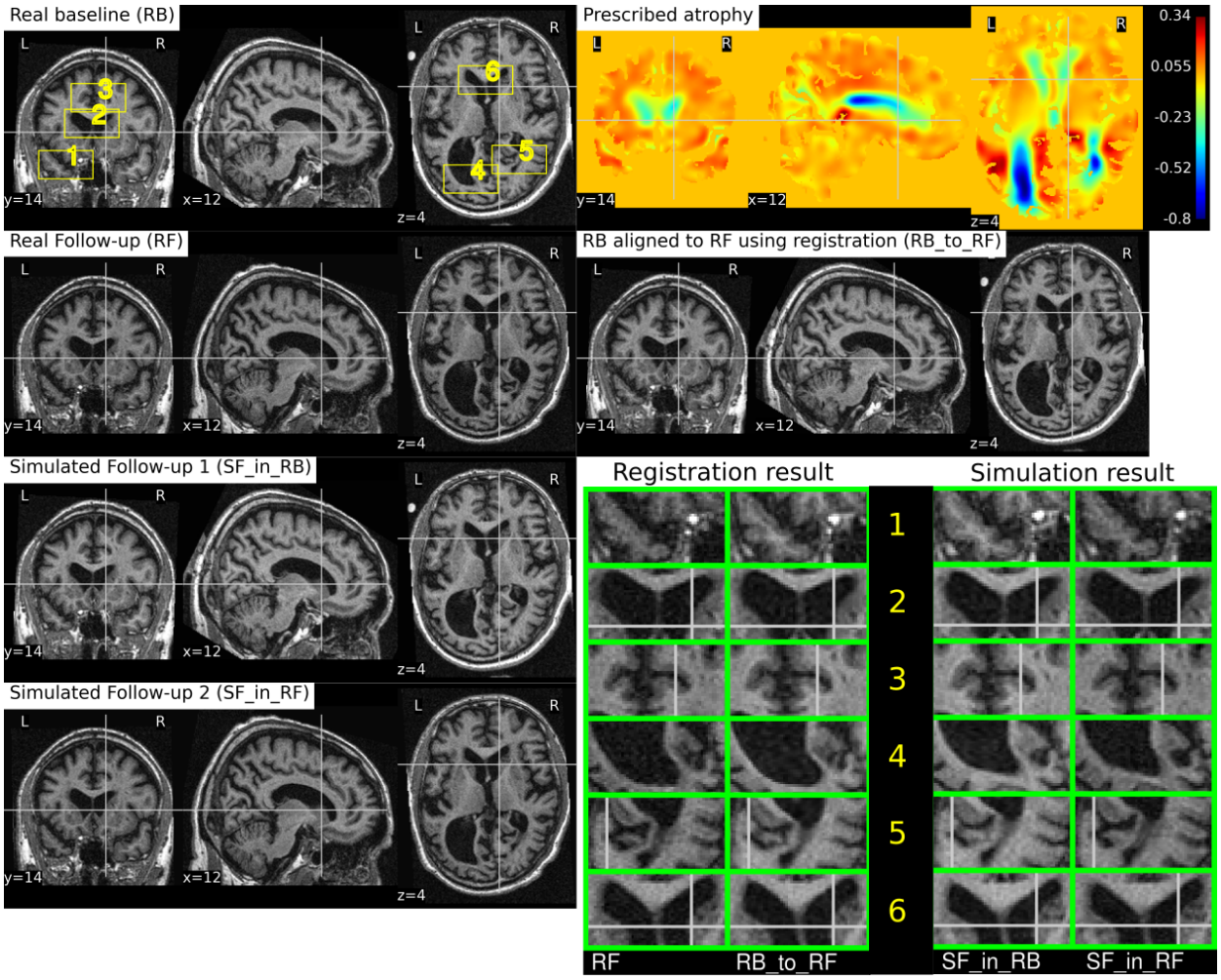

Figure 10: `RB` and `RF` are non-rigidly registered and the transformation obtained from the registration is used to align `RB` to `RF` which is shown in the image `RB_to_RF`. The figure also shows two simulated follow-up images `SF_in_RB` and `SF_in_RF` that are resampled from (`RB`) and (`RF`) respectively. We can see that in most regions of the brain, the two simulated images have almost identical morphological appearances. However, there are also regions such as 2 and 5, where the morphological appearances of the two simulated images are not identical. From the registration results for these regions 2 and 5 in the zoomed patches, we can see that the registration is also not accurate in those regions.

4.2. Discretization scheme for the divergence computation

In Khanal et al. (2016a), a standard staggered grid discretization was used for solving the system of Eqs. (1). The discretization scheme is shown in Figure 11 in 2D for illustration; explanation on 2D extends naturally to 3D. In the figure, we can see that the components of the displacement field variable $\mathbf{u}$ lie on cell faces and not at cell centres. However, all the input and output images for the model, including the output displacement field image, are standard images that have their values lying in cell centres or voxels. Our implementation of the solver internally creates the required staggered grid for the given input images. Once $\mathbf{u}$ is computed within the solver of system of Eqs.(1), its values at cell faces are interpolated

to obtain the values at cell centres which are then assembled to send as output displacement field image. Within the solver, the numerical scheme used for the discretization of $\nabla \cdot \mathbf{u} = -a$ is:

$$\frac{u_{i+1/2,j,k} - u_{i-1/2,j,k}}{h_x} + \frac{v_{i,j+1/2,k} - v_{i,j-1/2,k}}{h_y} + \frac{w_{i,j,k+1/2} - w_{i,j,k-1/2}}{h_z} = a_{i,j,k} \tag{2}$$

where,

$$\mathbf{u} = \begin{pmatrix} u \\ v \\ w \end{pmatrix}.$$

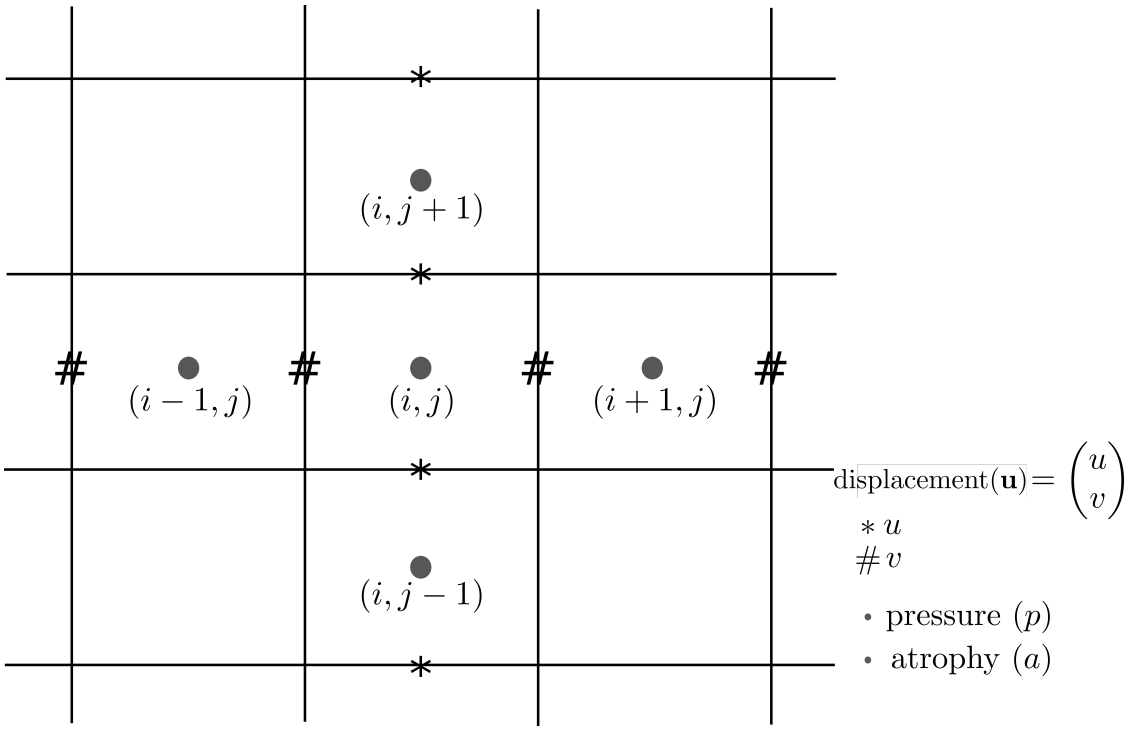

Figure 11: Standard staggered grid discretization scheme that is used to solve the system of Eqs. (1). Displacement variables are at faces (edges in 2D) of the cells, while pressure and atrophy values are at centres of the cells.

`Simul@trophy` then provides output displacement field image with the values of $\mathbf{u}$ lying at cell centres or voxels by using linear interpolation as follows:

$$\begin{pmatrix} u_{i,j,k} \\ v_{i,j,k} \\ w_{i,j,k} \end{pmatrix} = \begin{pmatrix} \left(u_{i+1/2,j,k} + u_{i-1/2,j,k}\right)/2 \\ \left(v_{i,j+1/2,k} + v_{i,j-1/2,k}\right)/2 \\ \left(w_{i,j,k+1/2} + w_{i,j,k-1/2}\right)/2 \end{pmatrix} \tag{3}$$

To compare divergence maps of this output field with the ones obtained from tools external of `Simul@trophy`, the only accessible values are the interpolated ones. ITK is

widely used in registration based brain morphometry algorithms, but the default derivative computation of ITK has the following centred difference stencil:

$$\frac{u_{i+1,j,k} - u_{i-1,j,k}}{2 * h_x} + \frac{v_{i,j+1,k} - v_{i,j-1,k}}{2 * h_y} + \frac{w_{i,j,k+1} - w_{i,j,k-1}}{2 * h_z} = a_{i,j,k} \tag{4}$$

Replacing the components of $\mathbf{u}$ at cell centres from Eq. 3, we get,

$$\frac{u_{i+3/2,j,k} + u_{i+1/2,j,k} - (u_{i-1/2,j,k} + u_{i+3/2,j,k})}{4 * h_x} + ... = a_{i,j,k} \tag{5}$$

The scheme in Eq. (5) does not match the one that was used internally by `Simul@trophy` shown in Eq. (2). This results in discrepancy if we compare input prescribed atrophy maps against the externally computed divergence maps $\nabla \cdot \mathbf{u}$. Thus, in this work, we have added an implementation for the scheme in Eq. (5) so that users can choose either of the two possible schemes of Eq. (2) and Eq. (5). The latter scheme is consistent with the divergence computed by the default derivative computation options of ITK. At each 3D cell, the scheme in Eq. (2) involves 6 variables of the displacement field, while the scheme in Eq. (5) involves 12 variables. In the rest of the paper, they will be referred to as `6-point` and `12-point` schemes respectively.

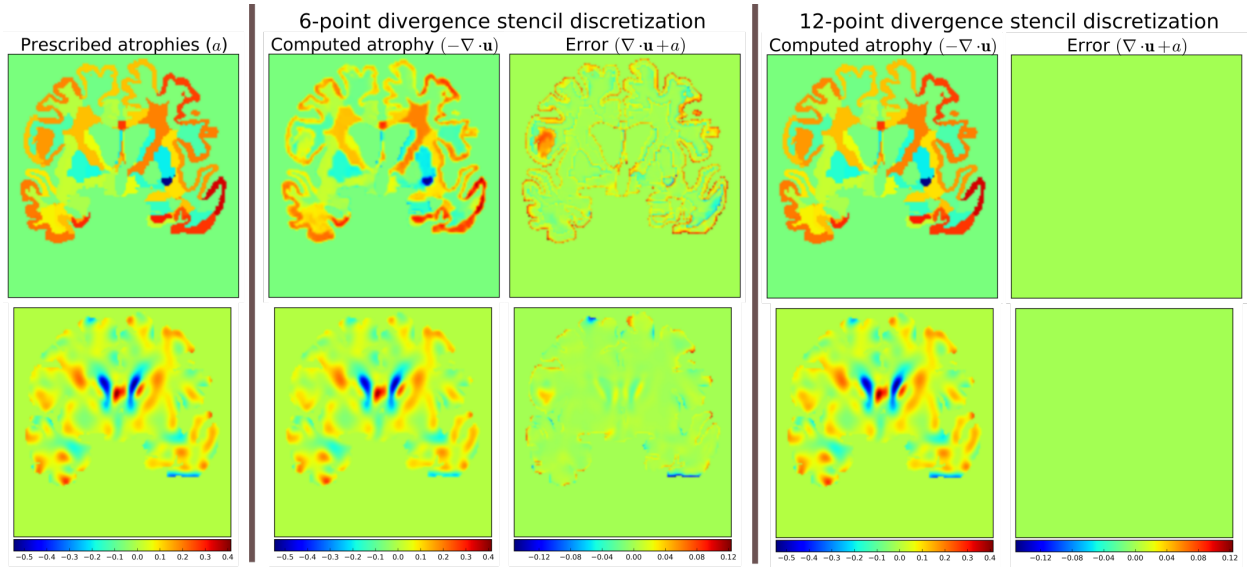

Figure 12: Error due to non-consistent numerical schemes in Eq. (2), and Eqs. (4 and 5). $\nabla \cdot \mathbf{u}$ shown in the figure are computed external of `Simul@trophy` by using the default ITK derivative computation scheme shown in Eq. (4). When this divergence computation is consistent with the one used in `Simul@trophy`, we should obtain zero error with $\nabla \cdot \mathbf{u} + a = 0$. This is indeed the case, as seen on the right, when we use `12-point` stencil of Eq. 5. We see non-zero errors when using `6-point` stencil from Eq. (2) because this scheme and the default ITK scheme are not consistent. The figure shows that the error gets larger at areas where prescribed atrophy has discontinuous jumps.

Figure 12 shows the error in specified vs. obtained atrophy when using the two different numerical schemes. As expected, we can see that when a consistent numerical scheme is

used, there is no difference between the specified and obtained atrophy. When the schemes are not consistent, the error is larger on the areas where the prescribed atrophy values change sharply.

If the simulated ground truth images using `Simul@trophy` are used for the evaluation of atrophy estimation algorithms, one must also be careful about the measure of volume change used in addition to the numerical scheme used. For instance, many TBM based brain morphometry algorithms use Jacobian determinants as a measure of volume change. To compute ground truth volume changes of the simulated images for the evaluation of such algorithms, users should compute Jacobian determinants of the output displacement fields $\mathbf{u}$ obtained from `Simul@trophy` by using the same numerical scheme as used by the atrophy estimation algorithm being evaluated.

4.3. Implementation of image warping

When implementing an algorithm to warp an image with a given deformation field, it is more convenient to use the inverse of the deformation field. If Φ_s is the output deformation field obtained from the brain deformation model by using I_b as the input baseline image, Φ_s maps any point $\mathbf{x}$ in I_b to a point $\mathbf{y}$ in the simulated image I_s as follows:

$$\mathbf{y} = \Phi_s(\mathbf{x}).$$

However, $\mathbf{y}$ is not guaranteed to be a discrete voxel location. Since we do not know the intensity values of I_s *a priori* in the nearby discrete positions, the problem of interpolation is much more complex. Thus, we start from a discrete voxel location $\mathbf{y}$ in I_s where the value of intensity is to be found. Then, the corresponding position $\mathbf{x}$ in I_b can be obtained by using the inverse deformation field:

$$\mathbf{x} = \Phi_s^{-1}(\mathbf{y}).$$

If the transformed point $\mathbf{x}$ is not a discrete point, we can interpolate the intensities of I_b from neighbouring discrete locations. Let us denote the interpolation by square brackets. Thus $i = I[\mathbf{x}]$ describes a mapping of a point $\mathbf{x}$ to an intensity, i, of the MR image I at $\mathbf{x}$. Using this notation, the intensity of the simulated image at any position $\mathbf{x}$ is given by:

$$I_b\left[\Phi_s^{-1}(\mathbf{x})\right].$$

The simulator must be provided with the option `invert_field_to_warp` to invert the field obtained from the model before warping the input baseline image.

```
--invert_field_to_warp  #Invert u; default: do not invert
```

The implementation of the inversion is adapted from a fixed-point scheme implementation available in ITK (Luethi, 2010). By default, the simulator uses B-spline interpolation of order three to warp the input images.

4.4. Standalone utility tools and scripts for pre-processing and post-processing

There are some standalone tools and scripts available for various pre-processing and post-processing operations that are detailed in the documentation of the released software.

Some of these tools for pre-processing and post-processing operations are C++ executables based on ITK, while others are python scripts. In this work, all the input segmentation of the model were obtained by using FreeSurfer. As explained in Khanal et al. (2016a), these segmentation maps were processed to obtain in the format required by the model. Although the provided scripts are developed for FreeSurfer segmentation maps, they can be easily modified to adapt to other pre-processing tools. Finally, the registration and simulation deformations were composed using `ComposeMultiTransform` of Advanced Neuroimaging Tools (ANTs) (Avants et al., 2011).

The core component of `Simul@trophy` is the implementation of the brain deformation model. Resampling of the intensity is straightforward once the deformations from the model and from registration are available. The simulator is not dependent on any one particular registration algorithm. Although we used LCC-LogDemons for illustrative purposes, this can be replaced with any other non-rigid registration algorihtms. Similarly pre-processing is also independent of `Simul@trophy`. We used FreeSurfer in the simulation examples shown in this work, but any other skull stripping and segmentation algorithms can be used. `Simul@trophy` provides some example scripts and some utility scripts, which could be modified when using other tools for the pre-processing step.

5. Discussion

In Khanal et al. (2016a), we presented a method to generate a subject-specific atrophy pattern by first measuring the atrophy from the available time-points, and then simulating a new time-point by prescribing the measured atrophy. In Khanal et al. (2016b), we extended the method to interpolate an unavailable intermediate time-point MRI. In this work, we added realistic variation in the intensity of the synthetic images. The simulation examples were shown using three types of atrophy patterns: i) very simple uniform volume changes in small number of regions, ii) uniform atrophy in large number of regions, and iii) smoothly varying atrophy patterns. For each subject, we could generate large number of synthetic images by perturbing these atrophy patterns in different ways. Even with the same atrophy pattern, we can generate multiple sets of longitudinal sequences of varying intensity characteristics using the approach illustrated in Figure 4. Thus, by changing the atrophy patterns and the image intensities, `Simul@trophy` could be used to generate a database of very large number of simulated images. Such a database might be useful for training of machine learning algorithms.

`Simul@trophy` can be used in evaluating atrophy estimation algorithms in similar ways as done by Pieperhoff et al. (2008); Camara et al. (2008); Sharma et al. (2010). The ability to prescribe atrophy at any time point allows the user to introduce volume changes at different regions of the brain at different times. Thus, another interesting application of the simulator is to train and/or validate disease progression models such as the models proposed in Chen

et al. (2012); Fonteijn et al. (2012); Jedynak et al. (2012); Dukart et al. (2013); Schmidt-Richberg et al. (2016). Having a database of longitudinal MRIs with known spatio-temporal distribution of atrophy can be useful to validate such algorithms. Furthermore, since the algorithms use a data driven approach, the simulator could be useful to train or fine-tune such models.

Another possible application is in filling up unavailable time-point MRIs of some of the subjects, when performing group-wise longitudinal analysis. In such studies, usually the available time-point images of each subject are used to estimate subject-specific volume changes. These subject-specific measurements are then used to perform group-wise statistics to check whether there are significant differences amongst different groups in some particular regions of the brain. Databases used in such analyses, might not always have all the required time-point images for all the subjects. This could lead to bias if all the subjects are not aligned properly in the temporal dimension of disease progression. Simulating new time-point images for some subjects and using them in the analysis might allow evaluating the impact of such mis-alignments.

We hope to promote two directions of research in the community with open-source release of `Simul@trophy`. *First*, the public availability of `Simul@trophy` enables researchers to build their own simulated databases as needed. This might also hopefully lead to a large public database of ground truth simulated images, that could be used for benchmarking and evaluation of various image based morphometry tools. *Second*, we hope that `Simul@trophy` allows other researchers to build upon the biophysical model we presented in Khanal et al. (2016a), and investigate further, providing more accurate models of brain atrophy.

Finally, `Simul@trophy` is general enough to be used for other imaging modalities such as CT scans. It could also be used with images of any other organs, where one requires simulating specified volume changes. In this case, the pre-processing should be changed accordingly to generate a segmentation image and atrophy maps. Thus, once the software is public, other researchers might find it useful in applications that we have not foreseen yet.

6. Conclusions

We proposed a simulation framework that can generate realistic longitudinal MRIs with specified volume changes. The framework allows generating large number of subject-specific multiple time-point images based on a biophysical model of brain deformation due to atrophy. We developed an open-source software `Simul@trophy` to implement the proposed framework. The core part of `Simul@trophy` is the implementation of our brain deformation model presented in Khanal et al. (2016a). `Simul@trophy` is based on widely used state of the art libraries PETSc (for solving large systems of equations) and ITK (for medical image processing). Since the software is publicly available in an open-source repository, we hope that researchers can use it to create databases of ground truth images. The framework could be used to generate a common public database, which in turn could be used to validate and evaluate a large number of available atrophy estimation algorithms. Similarly, these databases could be valuable for data driven disease progression models including machine learning algorithms. Validation and training of the models that study temporal

relationships, ordering and co-evolution of atrophy in different structures of the brain could be another interesting application.

Acknowledgments

1. We would like to thank Mehdi Hadj-Hamou for providing us registration results and the associated deformation fields that were used in this paper to resample intensity from different images. The preprocessing steps involved for this registration are explained in Hadj-Hamou et al. (2016).
2. Part of this work was funded by the European Research Council through the ERC Advanced Grant MedYMA 2011-291080.
3. This work benefited from the use of the Insight Segmentation and Registration Toolkit (ITK), an open source software developed as an initiative of the U.S. National Library of Medicine and available at www.itk.org.
4. The multi-platform configuration tool CMake was used for configuring ITK and facilitating its use from our project. CMake was partially funded by the U.S. National Library of Medicine as part of the Insight Toolkit project. CMake is an open source system and it is freely available at www.cmake.org.

7. Appendix

7.1. Running `Simul@trophy` *from command lines*

Once the pre-processing steps described in Section 2.1 are performed and the desired atrophy map is generated, these images can be used as input to the model by providing the following command line arguments:

```
-atrophyFile            #Input atrophy map
-maskFile               #Input segmentation file
-imageFile              #Input image file
```

If the model parameters μ and λ have uniform values in `Label1` and `Label2`, they can be provided as an argument to the option `-parameters`. On the other hand, if they need to have different values in different parts of the brain, one needs to provide them as images similar to other input images as shown below:

```
-parameters             #μ,λ in Region1, Region2. Format: μ1,μ2,λ1,λ2
-muFile                 #Ignore μ from -parameters, use this image
-lambdaFile             #Ignore λ from -parameters, use this image
--useTensorLambda       #λ given as DTI; default is scalar image
```

Some of the important options available are:

```
-boundary_condition     #dirichlet_at_walls or dirichlet_at_skull
--div12pt_stencil       #Use 12-point scheme; default: 6-point scheme
--relax_ic_in_csf       #Region1: ∇·u+kp=0; default is ∇·u=−a
-relax_ic_coeff         #Value of k
-numOfTimeSteps         #Number of time-steps to solve for
```

To solve the system of Eqs. (1), the argument to `-boundary_condition` should be `dirichlet_at_skull` and `--relax_ic_in_csf` must be provided. Using `dirichlet_at_walls` instead of `dirichlet_at_skull` will consider regions with `label0` in the same way as the regions with `label2`, and sets the Dirichlet boundary conditions only at the image borders.

If `-numofTimeSteps` is greater than one, the simulator provides an output displacement field obtained by composing output displacement fields of each time-steps. For any time-step `n` $<$ `numOfTimeSteps`, it also provides output synthetic image by warping the input image with the displacement field obtained by composing output displacement fields from time-step 1 to `n`. In addition to these outputs, if desired, some other extra outputs can be generated as shown below:

```
-resPath                 #Result path to store all the results
-resultsFilenamesPrefix  #Prefix to be provided to all the images
--writePressure          #Write p as image to disk.
--writeForce             #Write (μ + λ)∇a as image to disk.
--writeResidual          #Write solver residual as image to disk.
```

References

John Ashburner. Symmetric diffeomorphic modeling of longitudinal structural MRI. *Frontiers in Neuroscience*, 6, 2013. doi: 10.3389/fnins.2012.00197. URL `http://dx.doi.org/10.3389/fnins.2012.00197`.

John Ashburner and Karl J. Friston. Voxel-based morphometry—the methods. *NeuroImage*, 11(6):805 – 821, 2000. ISSN 1053-8119. doi: 10.1006/nimg.2000.0582. URL `http://www.sciencedirect.com/science/article/pii/S1053811900905822`.

John Ashburner and Gerard R. Ridgway. Tensor-based morphometry. In Arthur W Toga, editor, *Brain Mapping: An Encyclopedic Reference*, pages 383–394. Academic Press: Elsevier, feb 2015. ISBN 978-0-12-397316-0. doi: 10.1016/B978-0-12-397025-1.00309-2.

Brian Avants, Hans J Johnson, and Nicholas James Tustison. Neuroinformatics and the the insight toolkit. *Frontiers in Neuroinformatics*, 9(5), 2015. ISSN 1662-5196. doi: 10.3389/fninf.2015.00005. URL `http://www.frontiersin.org/neuroinformatics/10.3389/fninf.2015.00005/full`.

Brian B. Avants, Nicholas J. Tustison, Gang Song, Philip A. Cook, Arno Klein, and James C. Gee. A reproducible evaluation of ants similarity metric performance in brain image registration. *NeuroImage*, 54(3):2033 – 2044, 2011. ISSN 1053-8119. doi: http://dx.doi.org/10.1016/j.neuroimage.2010.09.025. URL `http://www.sciencedirect.com/science/article/pii/S1053811910012061`.

S. Balay, J. Brown, K. Buschelman, W. D. Gropp, D. Kaushik, M. G. Knepley, L. Curfman McInnes, B. F. Smith, and H. Zhang. PETSc Web page, 2013. http://www.mcs.anl.gov/petsc.

O. Camara, M. Schweiger, R. I. Scahill, W. R. Crum, B. I. Sneller, J. A. Schnabel, G. R. Ridgway, D. M. Cash, D. L. G. Hill, and N. C. Fox. Phenomenological model of diffuse global and regional atrophy using finite-element methods. *IEEE Transactions on Medical Imaging*, 25(11):1417–30, nov 2006. ISSN 0278-0062. doi: 10.1109/TMI.2006.880588. URL `http://www.ncbi.nlm.nih.gov/pubmed/17117771`.

Oscar Camara, Julia A Schnabel, Gerard R Ridgway, William R Crum, Abdel Douiri, Rachael I Scahill, Derek LG Hill, and Nick C Fox. Accuracy assessment of global and local atrophy measurement techniques with realistic simulated longitudinal alzheimer's disease images. *NeuroImage*, 42(2):696–709, 2008.

Owen Carmichael, Donald G. McLaren, Douglas Tommet, Dan Mungas, and Richard N. Jones. Coevolution of brain structures in amnestic mild cognitive impairment. *NeuroImage*, 66:449–456, feb 2013. doi: 10.1016/j.neuroimage.2012.10.029. URL `http://dx.doi.org/10.1016/j.neuroimage.2012.10.029`.

Rong Chen, Susan M. Resnick, Christos Davatzikos, and Edward H. Herskovits. Dynamic bayesian network modeling for longitudinal brain morphometry. *NeuroImage*, 59(3):2330 – 2338, 2012. ISSN 1053-8119. doi:

http://dx.doi.org/10.1016/j.neuroimage.2011.09.023. URL http://www.sciencedirect.com/science/article/pii/S105381191101069X.

Juergen Dukart, Ferath Kherif, Karsten Mueller, Stanislaw Adaszewski, Matthias L. Schroeter, Richard S. J. Frackowiak, Bogdan Draganski, and for the Alzheimer's Disease Neuroimaging Initiative. Generative fdg-pet and mri model of aging and disease progression in alzheimer's disease. *PLoS Comput Biol*, 9 (4):1–11, 04 2013. doi: 10.1371/journal.pcbi.1002987. URL http://dx.doi.org/10.1371%2Fjournal.pcbi.1002987.

Bruce Fischl, David H. Salat, Evelina Busa, Marilyn Albert, Megan Dieterich, Christian Haselgrove, Andre van der Kouwe, Ron Killiany, David Kennedy, Shuna Klaveness, Albert Montillo, Nikos Makris, Bruce Rosen, and Anders M. Dale. Whole Brain Segmentation: Automated Labeling of Neuroanatomical Structures in the Human Brain. *Neuron*, 33(3):341–355, jan 2002. ISSN 0896-6273. doi: 10.1016/S0896-6273(02)00569-X. URL http://www.sciencedirect.com/science/article/pii/S089662730200569X.

Hubert M. Fonteijn, Marc Modat, Matthew J. Clarkson, Josephine Barnes, Manja Lehmann, Nicola Z. Hobbs, Rachael I. Scahill, Sarah J. Tabrizi, Sebastien Ourselin, Nick C. Fox, and Daniel C. Alexander. An event-based model for disease progression and its application in familial Alzheimer's disease and Huntington's disease. *NeuroImage*, 60(3):1880–1889, apr 2012. doi: 10.1016/j.neuroimage.2012.01.062. URL http://dx.doi.org/10.1016/j.neuroimage.2012.01.062.

P. A. Freeborough and N. C. Fox. The boundary shift integral: an accurate and robust measure of cerebral volume changes from registered repeat mri. *IEEE Transactions on Medical Imaging*, 16(5):623–629, Oct 1997. ISSN 0278-0062. doi: 10.1109/42.640753.

G. B. Frisoni, N. C. Fox, C. R. Jack, P. Scheltens, and P. M. Thompson. The clinical use of structural MRI in Alzheimer disease. *Nature Reviews. Neurology*, 6(2):67–77, feb 2010. ISSN 1759-4766. doi: 10.1038/nrneurol.2009.215. URL http://www.pubmedcentral.nih.gov/articlerender.fcgi?artid=2938772&tool=pmcentrez&rendertype=abstract.

Krzysztof Jacek Gorgolewski, Gael Varoquaux, Gabriel Rivera, Yannick Schwartz, Satrajit S Ghosh, Camille Maumet, Vanessa V Sochat, Thomas E. Nichols, Russell A. Poldrack, Jean-Baptiste Poline, Tal Yarkoni, and Daniel S. Margulies. Neurovault.org: A web-based repository for collecting and sharing unthresholded statistical maps of the human brain. *Frontiers in Neuroinformatics*, 9(8), 2015. ISSN 1662-5196. doi: 10.3389/fninf.2015.00008. URL http://www.frontiersin.org/neuroinformatics/10.3389/fninf.2015.00008/abstract.

Hákon Gudbjartsson and Samuel Patz. The Rician Distribution of Noisy MRI Data. *Magnetic resonance in medicine : official journal of the Society of Magnetic Resonance in Medicine / Society of Magnetic Resonance in Medicine*, 34(6):910–914, December 1995. ISSN 0740-3194. URL http://www.ncbi.nlm.nih.gov/pmc/articles/PMC2254141/.

Mehdi Hadj-Hamou, Marco Lorenzi, Nicholas Ayache, and Xavier Pennec. Longitudinal analysis of image time series with diffeomorphic deformations: a computational framework based on stationary velocity fields. *Frontiers in Neuroscience*, 10(236), 2016. ISSN 1662-453X. doi: 10.3389/fnins.2016.00236. URL http://www.frontiersin.org/brain_imaging_methods/10.3389/fnins.2016.00236/abstract.

Xue Hua, Alex D. Leow, Neelroop Parikshak, Suh Lee, Ming-Chang Chiang, Arthur W. Toga, Clifford R. Jack Jr, Michael W. Weiner, and Paul M. Thompson. Tensor-based morphometry as a neuroimaging biomarker for alzheimer's disease: An {MRI} study of 676 ad, mci, and normal subjects. *NeuroImage*, 43(3):458 – 469, 2008. ISSN 1053-8119. doi: http://dx.doi.org/10.1016/j.neuroimage.2008.07.013. URL http://www.sciencedirect.com/science/article/pii/S1053811908008380.

Bruno M. Jedynak, Andrew Lang, Bo Liu, Elyse Katz, Yanwei Zhang, Bradley T. Wyman, David Raunig, C. Pierre Jedynak, Brian Caffo, and Jerry L. Prince. A computational neurodegenerative disease progression score: Method and results with the alzheimer's disease neuroimaging initiative cohort. *NeuroImage*, 63(3):1478 – 1486, 2012. ISSN 1053-8119. doi: http://dx.doi.org/10.1016/j.neuroimage.2012.07.059. URL http://www.sciencedirect.com/science/article/pii/S1053811912007896.

Mark Jenkinson and Stephen Smith. A global optimisation method for robust affine registration of brain images. *Medical Image Analysis*, 5(2):143 – 156, 2001. ISSN 1361-8415. doi: http://dx.doi.

org/10.1016/S1361-8415(01)00036-6. URL http://www.sciencedirect.com/science/article/pii/S1361841501000366.

B. Karaçali and C. Davatzikos. Simulation of tissue atrophy using a topology preserving transformation model. *IEEE Transactions on Medical Imaging*, 25(5):649–52, may 2006. ISSN 0278-0062. doi: 10.1109/TMI.2006.873221. URL http://www.ncbi.nlm.nih.gov/pubmed/16689268.

Bishesh Khanal, Marco Lorenzi, Nicholas Ayache, and Xavier Pennec. A Biophysical Model of Shape Changes due to Atrophy in the Brain with Alzheimer's Disease. In Polina Golland, Nobuhiko Hata, Christian Barillot, Joachim Hornegger, and Robert Howe, editors, *Medical Image Computing and Computer-Assisted Intervention – MICCAI 2014*, volume 8674 of *Lecture Notes in Computer Science*, pages 41–48. Springer International Publishing, 2014. ISBN 978-3-319-10469-0. doi: 10.1007/978-3-319-10470-6_6. URL http://dx.doi.org/10.1007/978-3-319-10470-6_6.

Bishesh Khanal, Marco Lorenzi, Nicholas Ayache, and Xavier Pennec. A biophysical model of brain deformation to simulate and analyze longitudinal mris of patients with alzheimer's disease. *NeuroImage*, 134:35 – 52, 2016a. ISSN 1053-8119. doi: http://dx.doi.org/10.1016/j.neuroimage.2016.03.061. URL http://www.sciencedirect.com/science/article/pii/S1053811916300052.

Bishesh Khanal, Marco Lorenzi, Nicholas Ayache, and Xavier Pennec. Simulating patient specific multiple time-point mris from a biophysical model of brain deformation in alzheimer's disease. In Grand Joldes, Barry Doyle, Adam Wittek, Poul M. F. Nielsen, and Karol Miller, editors, *Computational Biomechanics for Medicine: Imaging, Modeling and Computing*. Springer International Publishing AG, May 2016b. ISBN 9783319283272.

Kathrin Koch, Tim Jonas Reess, Oana Georgiana Rus, and Claus Zimmer. Extensive learning is associated with gray matter changes in the right hippocampus. *NeuroImage*, 125:627 – 632, 2016. ISSN 1053-8119. doi: http://dx.doi.org/10.1016/j.neuroimage.2015.10.056. URL http://www.sciencedirect.com/science/article/pii/S1053811915009672.

S. Langlois, M. Desvignes, J. M. Constans, and M. Revenu. MRI geometric distortion: a simple approach to correcting the effects of non-linear gradient fields. *Journal of magnetic resonance imaging: JMRI*, 9 (6):821–831, June 1999. ISSN 1053-1807.

M. Lorenzi, N. Ayache, G.B. Frisoni, and X. Pennec. LCC-Demons: A robust and accurate symmetric diffeomorphic registration algorithm. *NeuroImage*, 81:470–483, nov 2013. doi: 10.1016/j.neuroimage.2013.04.114. URL http://dx.doi.org/10.1016/j.neuroimage.2013.04.114.

M. Luethi. Inverting deformation fields using a fixed point iteration scheme. *The Insight Journal*, 10 2010.

Daniel S. Marcus, Anthony F. Fotenos, John G. Csernansky, John C. Morris, and Randy L. Buckner. Open access series of imaging studies: Longitudinal MRI data in nondemented and demented older adults. *Journal of Cognitive Neuroscience*, 22(12):2677–2684, 2010.

Matthew Michael McCormick, Xiaoxiao Liu, Luis Ibanez, Julien Jomier, and Charles Marion. Itk: Enabling reproducible research and open science. *Frontiers in Neuroinformatics*, 8(13), 2014. ISSN 1662-5196. doi: 10.3389/fninf.2014.00013. URL http://www.frontiersin.org/neuroinformatics/10.3389/fninf.2014.00013/abstract.

P. Pieperhoff, M. Südmeyer, L. Hömke, K. Zilles, A. Schnitzler, and K. Amunts. Detection of structural changes of the human brain in longitudinally acquired MR images by deformation field morphometry: methodological analysis, validation and application. *NeuroImage*, 43(2):269–87, nov 2008. ISSN 1095-9572. doi: 10.1016/j.neuroimage.2008.07.031. URL http://www.ncbi.nlm.nih.gov/pubmed/18706506.

Adityo Prakosa, Maxime Sermesant, Hervé Delingette, Stéphanie Marchesseau, Eric Saloux, Pascal Allain, Nicolas Villain, and Nicholas Ayache. Generation of synthetic but visually realistic time series of cardiac images combining a biophysical model and clinical images. *IEEE transactions on medical imaging*, 32(1): 99–109, January 2013. ISSN 1558-254X. doi: 10.1109/TMI.2012.2220375.

Howard J Rosen, Maria Luisa Gorno-Tempini, WP Goldman, RJ Perry, N Schuff, Michael Weiner, R Feiwell, JH Kramer, and Bruce L Miller. Patterns of brain atrophy in frontotemporal dementia and semantic dementia. *Neurology*, 58(2):198–208, 2002.

Alexander Schmidt-Richberg, Christian Ledig, Ricardo Guerrero, Helena Molina-Abril, Alejandro Frangi, Daniel Rueckert, and on behalf of the Alzheimer's Disease Neuroimaging Initiative. Learning biomarker

models for progression estimation of alzheimer's disease. *PLoS ONE*, 11(4):1–27, 04 2016. doi: 10.1371/journal.pone.0153040. URL http://dx.doi.org/10.1371%2Fjournal.pone.0153040.

Jorge Sepulcre, Jaume Sastre-Garriga, Mara Cercignani, Gordon T Ingle, David H Miller, and Alan J Thompson. Regional gray matter atrophy in early primary progressive multiple sclerosis: a voxel-based morphometry study. *Archives of neurology*, 63(8):1175–1180, 2006.

S. Sharma, V. Noblet, F. Rousseau, F. Heitz, L. Rumbach, and J.P. Armspach. Evaluation of brain atrophy estimation algorithms using simulated ground-truth data. *Medical Image Analysis*, 14(3):373–89, jun 2010. ISSN 1361-8423. doi: 10.1016/j.media.2010.02.002. URL http://www.ncbi.nlm.nih.gov/pubmed/20219411.

S. Sharma, F. Rousseau, F. Heitz, L. Rumbach, and J.P. Armspach. On the estimation and correction of bias in local atrophy estimations using example atrophy simulations. *Computerized Medical Imaging and Graphics*, 37(7–8):538 – 551, 2013. ISSN 0895-6111. doi: http://dx.doi.org/10.1016/j.compmedimag.2013.07.002. URL http://www.sciencedirect.com/science/article/pii/S0895611113001316.

J. G. Sled, A. P. Zijdenbos, and A. C. Evans. A nonparametric method for automatic correction of intensity nonuniformity in MRI data. *IEEE transactions on medical imaging*, 17(1):87–97, February 1998. ISSN 0278-0062. doi: 10.1109/42.668698.

A. D. C. Smith, W. R. Crum, D. L. Hill, N. A. Thacker, and P. A. Bromiley. Biomechanical simulation of atrophy in MR images. In *Medical Imaging 2003*, pages 481–490. International Society for Optics and Photonics, 2003.

Stephen M Smith, Yongyue Zhang, Mark Jenkinson, Jacqueline Chen, PM Matthews, Antonio Federico, and Nicola De Stefano. Accurate, robust, and automated longitudinal and cross-sectional brain change analysis. *Neuroimage*, 17(1):479–489, 2002.

Jennifer L Whitwell and Clifford R Jack Jr. Comparisons between alzheimer disease, frontotemporal lobar degeneration, and normal aging with brain mapping. *Topics in Magnetic Resonance Imaging*, 16(6):409–425, 2005.

I.C. Wright, P.K. McGuire, J.-B. Poline, J.M. Travere, R.M. Murray, C.D. Frith, R.S.J. Frackowiak, and K.J. Friston. A voxel-based method for the statistical analysis of gray and white matter density applied to schizophrenia. *NeuroImage*, 2(4):244 – 252, 1995. ISSN 1053-8119. doi: http://dx.doi.org/10.1006/nimg.1995.1032. URL http://www.sciencedirect.com/science/article/pii/S1053811985710324.